Cement & Concrete Composites 30 (2008) 938–946

Contents lists available at ScienceDirect

Cement & Concrete Composites

journal homepage: www.elsevier.com/locate/cemconcomp

Response of ultra-high performance fiber reinforced concrete (UHPFRC) to impact and static loading

Katrin Habel [a,*], Paul Gauvreau [b]

[a] AECOM Canada, 17007 107 Ave, Edmonton, Alberta, Canada, T6E 2G3
[b] University of Toronto, Department of Civil Engineering Toronto, Ontario, Canada

ARTICLE INFO

Article history:
Received 16 March 2007
Received in revised form 1 September 2008
Accepted 1 September 2008
Available online 11 September 2008

Keywords:
Ultra-high performance fiber reinforced concrete (UHPFRC)
Impact tests
Static tests
High strain rates
Analytical modeling
Mass–spring models

ABSTRACT

This paper presents an experimental and analytical study of rate-dependent ultra-high performance fiber reinforced concrete (UHPFRC) behavior. UHPFRC three- and four-point bending response was determined on plates subjected to quasi-static loading. Drop weight tests were performed in order to apply dynamic three-point-bending loading to UHPFRC plates. In addition, uniaxial tensile tests were performed at different strain rates. A cross-sectional bending model related the uniaxial tensile behavior to the bending response with good agreement. The equivalent static response of the plate specimens in the drop weight tests was successfully determined with nonlinear mass–spring models. The results of this study show a significantly increased strength and fracture energy of the dynamically loaded plates when compared to quasi-static loading and confirm the validity of the analytical modeling.

1. Introduction

Ultra-high performance fiber reinforced concrete (UHPFRC) is a material with specifically tailored characteristics, resulting in excellent mechanical properties and a very low permeability. Its high strength (>130 MPa in compression and >8 MPa in tension) and strain hardening behavior under tensile loading make it resistant to severe loading and environmental action. Its dense matrix, in combination with the advantageous strain hardening behavior, leads to the very low permeability, which can improve the durability of UHPFRC structural members compared to conventional concrete members [1–5].

Previous studies have clearly shown the advantages from the use of high performance fiber reinforced cementitious composites (HPFRCC) such as UHPFRC, engineered cementitious composites (ECC) and slurry-infiltrated concrete (SIFCON) in structural members under static loading conditions [6–10]. Much less is known, however, about the behavior of HPFRCC under high strain rates [11–18].

It was observed that HPFRCC are more sensitive to the loading rate than conventional concrete: their strength gain is higher for increasing strain rates than for conventional concrete [11–13]. Strain capacity, however, does not appear to be affected by strain rate [12]. Moreover, these materials show improved structural behavior when compared to conventional concrete, and there was reduced spalling and scabbing under impact-type loading. The capacity of multiple cracking in HPFRCC leads to a high-energy dissipation and a high deformation capacity without provoking brittle fracture, as would be the case for conventional concrete [12,14]. However, the deformation capacity of HPFRCC is largely dependent on fiber length compared to crack width, since it is commonly known that force transfer through a given crack decreases to a small value as the crack width approaches one-half the fiber length.

The behavior of structural members subjected to high strain rates from dynamic loading can either be modeled numerically by finite element analyses or analytically by mass–spring models. While appropriate finite element models allow more refined analysis, mass–spring models are relatively simple and can be successfully used to simulate impact-type loading, when nonlinear springs are incorporated into the models [19–22]. Only analytical modeling based on mass–spring models was used in the study described in this paper.

The objectives of this study were to investigate experimentally the quasi-static and dynamic response of UHPFRC under high strain rates and to validate a proposed analytical modeling approach for this type of material. For this, the mechanical response of UHPFRC under bending was studied under quasi-static loading and under impact by drop weight tests. Also, some rate-dependent uniaxial tensile tests were performed. The response of

* Corresponding author. Tel.: +1 780 638 2182.
E-mail address: katrin.habel@aecom.com (K. Habel).

0958-9465/$ - see front matter © 2008 Elsevier Ltd. All rights reserved.
doi:10.1016/j.cemconcomp.2008.09.001

Nomenclature

E_{Uc}	Young's modulus of UHPFRC in compression
$E_{Ut,hard}$	strain hardening modulus of UHPFRC in tension
E_{Ut}	Young's modulus of UHPFRC in tension
F	force
F_{DW}	drop weight force determined from accelerometers
F_{su}	sum of the vertical support reactions from load cells
F_{Uc}	force in the compression zone of a UHPFRC bending member
F_{Ut}	force in the tension zone of a UHPFRC bending member
L	specimen span
L_{hi}	hinge length
L_R	reference length
M	bending moment
MOR	modulus of rupture
R_D	nonlinear spring representing the response of the plywood
R_P	nonlinear spring representing the response of the plate
a_{DW}	drop weight acceleration
b	specimen width
f_{Uc}	UHPFRC compressive strength
f_{Ut}	UHPFRC tensile strength
$f_{Ut,1st}$	cracking strength of UHPFRC in tension
$f1$	mid-span deflection
h_U	specimen depth
m_{DW}	drop weight mass
m_P	concentrated plate mass
$\bar{m}$	mass per unit length of the specimen
T	time
u_{DW}	drop weight displacement
u_P	plate displacement
w_{Ut}	crack width of a localized crack in the UHPFRC
$w_{Ut,1}$	parameter of the UHPFRC softening diagram
$w_{Ut,2}$	parameter of the UHPFRC softening diagram
x	depth of the compression zone
Φ	shape function
ε	strain
$d\varepsilon/dt$	strain rate
ε_{Uc}	UHPFRC compressive strain
$\varepsilon_{Uc,y}$	parameter of the UHPFRC compressive strength
$\varepsilon_{Uc,u}$	parameter of the UHPFRC compressive strength
ε_{Ut}	UHPFRC tensile strain
$\varepsilon_{Ut,1st}$	UHPFRC first cracking strain
$\varepsilon_{Ut,max}$	UHPFRC strain at the tensile strength
σ	stress
σ_1	parameter of the UHPFRC softening diagram
σ_{Uc}	compressive stress in the UHPFRC member
σ_{Ut}	tensile stress in the UHPFRC member

test specimens under static bending was modeled with an analytical model based on the UHPFRC compressive and tensile behaviors. An adequacy of a two mass–spring model to simulate the dynamic response of the drop weight tests was validated. The dynamic response was then compared to the results of the quasi-static tests.

2. Experimental program

2.1. Overview

The static and impact behavior of UHPFRC was determined in bending on 26 UHPFRC plate specimens. Each plate had a length of 600 mm, a width of 145 mm and a depth of 50 mm. Additional dog bone-shaped specimens with length 600 mm, width 100 mm and depth 50 mm were tested in direct tension for a range of strain rates.

2.2. Material composition and specimen preparation

The UHPFRC mix design was based on the composition developed by Rossi [2], and used locally available constituents. Mix proportions are provided in Table 1. The water/binder ratio was 0.20, with the binder including cement and silica fume. Additional details on the development of the mix are provided in [23]. The UHPFRC was mixed in a horizontal axis mortar mixer, using a batch size of 50 l. All plates were cast in three batches. Tests confirmed that the three batches produced similar material properties. The self-consolidating mix was placed into the formwork using a bucket. No heat or pressure treatments were utilized during casting or curing. The UHFPRC was cured under moist burlap and plastic for seven days. All specimens were then stored in a moist curing chamber at a temperature of 23 °C until testing. Compressive strength was determined using 100 mm diameter × 200 mm cylindrical specimens. The average strengths from three cylinder tests were 128, 132 and 131 MPa at 28, 90 and 253 days, respectively. All plate tests were conducted for specimen ages between 90 and 260 days. Since the mechanical properties were virtually constant for ages greater than 90 days, as shown with the compression tests in this study and in [24] using similar mix designs, the difference in test age did not significantly influence the test results.

Table 1
Composition of the UHPFRC

Constituent	Type	Weight (kg/m^3)
Cement	Portland cement	967
Silica fume	White, specific surface: 15–18 m^2/g	251
Silica sand	Size < 0.5 mm	675
Steel fibers	Straight (length/diameter: 10 mm/0.2 mm)	430
Superplasticizer	Polycarboxylate	35
Total water		244

2.3. Test setups

2.3.1. Uniaxial tensile tests

Four tests under uniaxial tension were performed on UHPFRC specimens cast in dog bone configurations having a reduced cross-section measuring 100 × 50 mm over a length of 300 mm. The tests were deformation-controlled by the mean value of two linear variable differential transformers (LVDT) placed at the sides of the specimens. Two specimens were loaded under quasi-static conditions at a strain rate of $d\varepsilon/dt = 8 \times 10^{-7}\ s^{-1}$, and one each at the higher strain rates of $d\varepsilon/dt = 5 \times 10^{-3}\ s^{-1}$ and $d\varepsilon/dt = 2 \times 10^{-2}\ s^{-1}$. These higher strain rates can be viewed as values representative of demand from seismic loading, or from vehicle impact on bridge piers [20]. The specimens were equipped with two LVDTs spanning the entire reduced cross-section on the back side. Force in the specimen and stroke of the testing machine were also measured. Further details on test method and results can be found in [25,26].

2.3.2. Quasi-static bending tests

Quasi-static three- and four-point bending tests were performed using the configurations shown in Fig. 1. The specimens

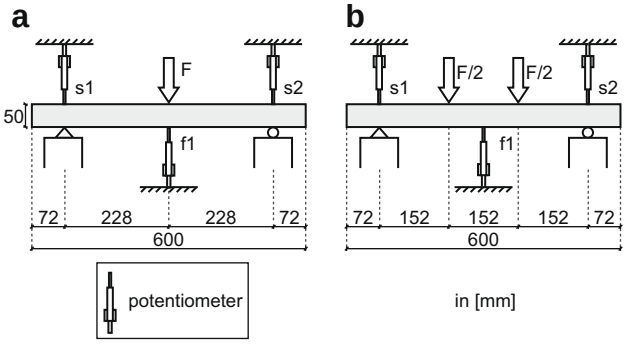

Fig. 1. Quasi-static bending test configurations: (a) three-point bending and (b) four-point bending.

were tested under displacement-control in a 1000 kN capacity universal testing machine at a loading rate of 6×10^{-6} m/s. Assuming linear–elastic material behavior, this corresponds to a strain rate in the lower extreme fiber of the plate of 5.7×10^{-6} s^{-1} at mid-span. Deflections were measured with linear potentiometers. The load and stroke of the machine were also recorded.

2.3.3. Bending tests under high strain rates

Drop weight tests were used to apply high strain rates to the specimens. The test configuration is illustrated in Fig. 2. Two drop weights of 10.2 and 20.6 kg, respectively, were used, from a constant drop height of 1050 mm measured between the top of the 19 mm thick, 20 mm wide plywood and the bottom of the drop weight. Vertical tie-down rods, prestressed with forces of 5 and 10 kN for the tests with the 10.3 and the 20.6 kg weights, respectively, were provided at both supports to prevent uplift of the specimens during rebound after the impact. To minimize horizontal restraint, free steel rollers were used at the underside of the plate. The rollers at the top of the plate and at the support beam below the load cell allowed rotation of the tie (see Fig. 2). The plywood was replaced after every drop. Multiple drops were performed on most specimens in order to obtain complete fracture.

Since some friction was produced between the drop weight and the steel guide frame, the speed of the drop weight at the instant of impact needed to be determined. This was accomplished through image analysis of digital movies recorded for each drop by a high-speed camera operating at 1000 frames per second. The speed at impact was evaluated to 4.2 m/s for the 10.3 kg weight and 4.3 m/s for the 20.6 kg weight.

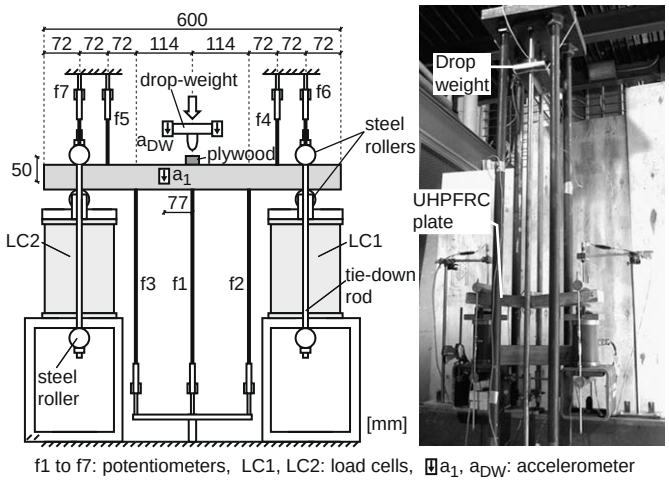

Fig. 2. Setup of the dynamic bending tests.

The impact force was determined from the average reading of two accelerometers (a_{DW}) affixed to the drop weight. Support reaction forces were measured with load cells (denoted LC1 and LC2 in Fig. 2). The strains in the tie-down rods were recorded from electrical resistance strain gauges. These strain gauges were previously calibrated to force values with tests in a uniaxial tension setup. Deflections were assessed at several locations with potentiometers (denoted $f1$–$f7$ in Fig. 2). Moreover, the vertical acceleration of the specimen was measured at one side at a location 77 mm from the mid-span with an accelerometer. Three specimens, impacted with the 10.3 kg weight, were equipped with electrical resistance strain gauges affixed to the concrete surface. The data acquisition rate for all instrumentation was 2.4 kHz. All specimens were visually inspected after every drop.

3. Analytical modeling

3.1. Overview

The objective of the modeling was to validate the approach of using analytical models to predict the response of UHPFRC flexure-critical members under quasi-static and impact-type loading. The models were also used for further understanding and interpretation of the test results.

A cross-sectional based model was used to describe the moment–curvature relationship based on the uniaxial tensile and compression properties. The moment–curvature relationship was then distributed over the length of the component. Localized cracks were modeled as hinges with a hinge length L_{hi}. Dynamic inertia effects were taken into account by a mass–spring model that allowed prediction of the dynamic response based on an equivalent force–deflection diagram of the component.

3.2. Cross-section based bending response model

The moment–curvature relationship was obtained with a cross-sectional model as shown in Fig. 3. The model is based on the plane sections hypothesis and is similar to the model presented in [27]. The crack width during the tension softening behavior of UHPFRC (Fig. 3b) was transformed into an equivalent strain by using a reference length L_R. The variation in the deflection along the length of the member was determined from the moment–curvature relationship, and force–deflection curves for the flexure-critical

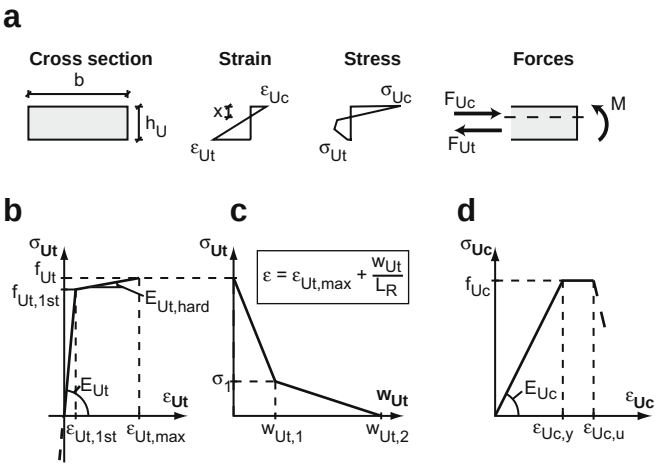

Fig. 3. Analytical cross-sectional model for UHPFRC under bending: (a) model definition, (b) linear–elastic and strain hardening in tension, (c) softening behavior of in tension and (d) compressive behavior.

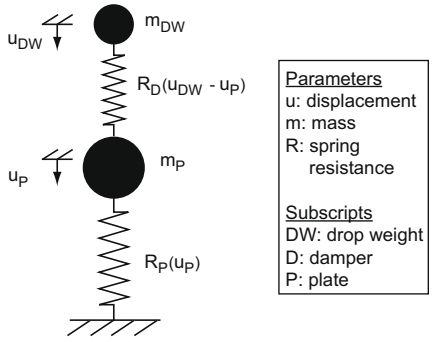

Fig. 4. Two mass–spring model of UHPFRC plate and plywood.

UHPFRC specimens were developed. For this, the beam was subdivided into 26 elements over its length. At locations of crack localization, a hinge length L_{hi} was defined, within which the deformation resulting from the crack opening was concentrated. Crack localization was assumed to occur when the tension chord exhibited softening.

3.3. Mass–spring model

The response of the UHPFRC plates under high strain rates was modeled with the nonlinear two mass–spring model shown in Fig. 4. The UHPFRC plate was simulated as a concentrated mass (m_P), which was determined by considering a shape function Φ according to

$$m_p = \int_0^l \bar{m} \cdot \Phi^2(x) \cdot dx \tag{1}$$

where m_P: concentrated plate mass, $\bar{m}$: mass per unit length of the specimen, Φ: shape function, L: span length.

The shape function is based on the deflected shape of the specimen. Mass–spring models like the one in this study are commonly used to determine the dynamic behavior of structural elements and are described in more detail, for example, in [19,20]. The well-known mathematical formulation of the model, including inertia effects, is given in Eqs. (2) and (3). The springs, represented by R_P and R_D, are nonlinear. The spring $R_P(u_P)$ represents the equivalent static force–deflection response of the plates, and the spring $R_D(u_{DW} - u_P)$ represents the force–displacement relationship of the plywood

$$m_{DW} \cdot \left(\frac{d^2 u_{DW}}{dt^2} - \frac{d^2 u_p}{dt^2} \right) + R_D(u_{DW} - u_p) = 0 \tag{2}$$

$$m_p \cdot \frac{d^2 u_p}{dt^2} + R_p(u_p) - R_D(u_{DW} - u_p) = 0 \tag{3}$$

with terms according to Fig. 4.

4. Results and discussion

4.1. Uniaxial tensile behavior

The results of the uniaxial tensile tests are presented in Fig. 5, which is subdivided in the two major domains that are typical for UHPFRC tensile behavior: (a) a linear–elastic and strain hardening part, which includes the linear–elastic stress rise and the strain hardening domain, and in which the energy dissipation can be seen as volumetric and (b) the softening part in which the energy is dissipated in a localized crack at the crack surface.

Fig. 5a shows the stress–strain relationship in the strain hardening part of the curve. The stress was calculated by dividing the measured force by the reduced cross-section of the dog bone (100 × 50 mm). Strain values were determined from the average displacement measured with the LVDTs which spanned over the entire reduced cross-section portion of the specimen. Fig. 5b provides the relation between stress and crack width (w) during softening. The crack width was directly obtained from the mean value of the two LVDTs spanning over the reduced cross-section of the specimen. Also the mean curve of the two tests with a strain rate of $d\varepsilon/dt = 8 \times 10^{-7}\ s^{-1}$ was calculated and plotted in Fig. 5.

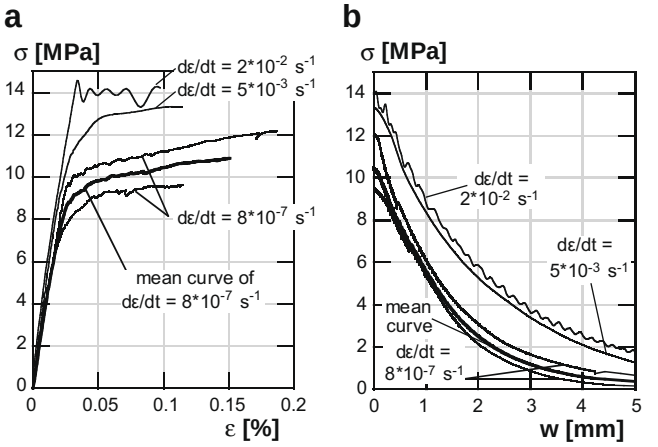

Fig. 5. UHPFRC uniaxial tensile behavior: (a) linear–elastic part and strain hardening and (b) softening.

The average apparent strain at the end of strain hardening region of the quasi-static tests was $\varepsilon_{Ut,max} = 0.15\%$ and the average tensile strength was $f_{Ut} = 11.0$ MPa. The two tests with the higher strain rates had a higher maximum force and lower strain hardening than the two tests with the lowest strain rate (Fig. 5a). Also, the slope of the stress–strain diagram $E_{Ut,hard}$ (see Fig. 3) decreased during strain hardening for higher strain rates. The tensile stress f_{Ut} increased by approximately 25% between strain rates of $d\varepsilon/dt = 5 \times 10^{-3}\ s^{-1}$ and $2 \times 10^{-2}\ s^{-1}$. For a strain rate of $d\varepsilon/dt = 2 \times 10^{-2}\ s^{-1}$, slight strain hardening was observed until a strain of $\varepsilon_{Ut,max} = 0.10\%$. Since energy dissipation can be seen as volumetric during strain hardening, the volumetric energy dissipation capacity decreased for increasing strain rates.

Softening behavior was also influenced by the strain rate (Fig. 5b): higher strain rates led to a slower decrease of the stress for increasing crack widths. During softening, energy dissipates in a localized crack as surface fracture energy.

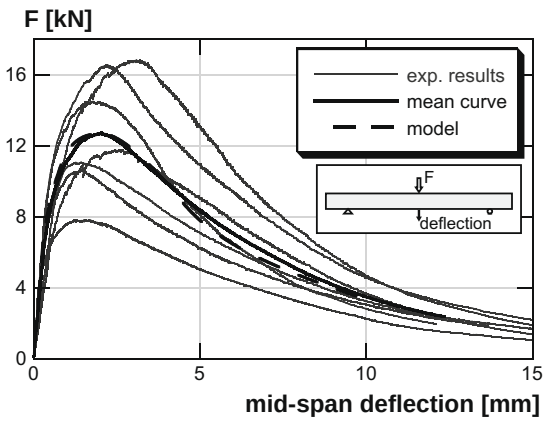

Fig. 6. Force–mid-span deflection curves from three-point bending tests.

Though limited in number, the tests show that UHPFRC performs well under higher strain rates: strength and fracture energy during softening were increased with higher strain rates. A slight reduction in strain hardening capacity with increased strain rate was also observed. The results are consistent with results found in the literature for ECC [12].

4.2. Quasi-static bending tests

The quasi-static response of UHPFRC was determined from three- and four-point bending tests. Applied force is plotted as a function of mid-span deflection in Figs. 7 and 8 for the three-point and four-point tests, respectively. Mid-span deflection was corrected for measured support settlements. Mean response of the tests and response computed using the cross-sectional analytical model are also plotted.

The average peak force for the seven three-point bending tests was 12.8 kN at a deflection of 2.0 mm. The scatter of the test results for maximum force and mid-span deflection was relatively high, with coefficients of variation of 25%. This scatter is believed to result from variations in both the fiber distribution within the matrix, which resulted from the mixing procedures, and casting method utilized. The horizontal axis mortar mixer used in this study resulted in slightly poorer mixing efficiency as compared to high-energy pan-type mixers normally used for producing UHPFRC. This factor, together with problems in the flow of the self-consolidating concrete within the moulds, and differences in fiber orientation within the moulds, may have contributed to variations in fiber alignment and distribution.

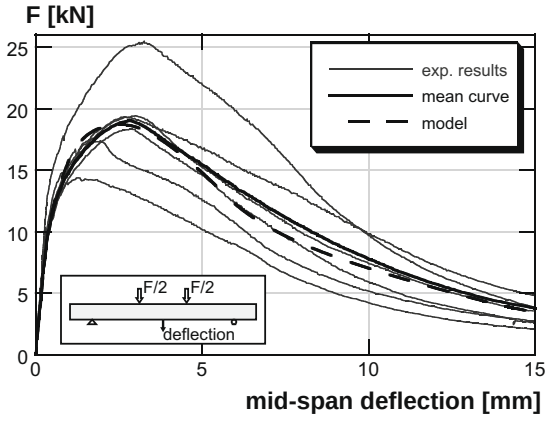

Fig. 7. Force–mid-span deflection curves from four-point bending tests.

The mean curves of the bending response of the three- and four-point bending specimens were modeled with the analytical cross-sectional model described in Section 3.2. A Young's modulus of $E_{Uc} = E_{Ut} = 40$ GPa and a compression strength of 130 MPa were assumed. As tensile input, the response of the quasi-static uniaxial tensile test was used, as shown in Fig. 8. The force–deformation curves generated by the analytical model were in good agreement with the mean test curves, as illustrated in Figs. 6 and 7. This demonstrates that it is possible to correlate the uniaxial tensile response to the bending response of UHPFRC.

For calculations of the moment–curvature response, the reference length used was $L_R = 120$ mm (Fig. 3) and the hinge length of $L_{hi} = 100$ mm and $L_{hi} = 130$ mm for the three- and four-point-bending specimens, respectively. Hinge length and reference length are both dependent on several material- and structure-related parameters as described in [10]. The lengths used in this study were selected empirically based on the experimental data, since a suitable rational determination is still in research and not the focus of the presented study. It can be seen that the hinge length for the four-point bending was longer than for three-point bending, which is consistent with what would be expected from the difference in the structural systems.

4.3. Drop weight bending tests

4.3.1. Experimental results

Thirteen drop weight tests were performed to determine the dynamic behavior of UHPFRC plates under bending (Table 2). In the table, the number of drops is defined as the number necessary for complete fracture of the specimen. The maximum strain rate (max. $d\varepsilon/dt$) in the lower fiber of the specimen was determined from the mid-span deflection history and by assuming linear–elastic material behavior.

The seven specimens impacted with the 10.3 kg weight were tested between three and five times each, while four of the six specimens impacted with the 20.6 kg weight failed during the first impact (Table 2). The scatter in the impact test results was comparable to the scatter of the quasi-static tests and was also attributed to varying fiber distributions in the specimens.

The maximum observed strain rates were approximately $d\varepsilon/dt = 2\ s^{-1}$. This was confirmed by the strain gauge measurements at the bottom side of the plates. The measured strain rate at the

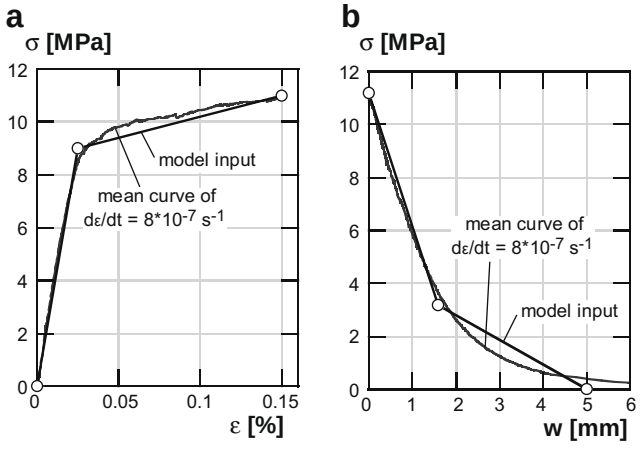

Fig. 8. UHPFRC tensile input for the modeling of the static bending tests: (a) linear–elastic part and strain hardening and (b) softening behavior.

Table 2
Summary of the drop weight tests

Specimen name (–)	Drop weight (kg)	Number of drops (–)	First drop			
			Max. $f1$ (mm)	Max. F_{DW} (kN)	Max. F_{su} (kN)	Max. $d\varepsilon/dt$ (s^{-1})
10kg_1	10.3	4	−4.1	23.0	24.5	2.5
10kg_2	10.3	5	−4.2	23.4	25.3	2.6
10kg_3	10.3	5	−4.6	22.8	26.4	3.0
10kg_4	10.3	3	−5.1	23.5	18.5	2.4
10kg_5	10.3	3	−5.1	21.6	16.7	2.8
10kg_6	10.3	3	−5.2	21.5	14.8	1.9
10kg_7	10.3	3	−5.7	23.3	20.9	2.7
20kg_1	20.6	2	−6.5	26.3	30.7	2.3
20kg_2	20.6	2	−12.2	23.4	19.7	3.1
20kg_3	20.6	1	–[a]	23.0	14.3	3.5
20kg_4	20.6	1	–[a]	23.8	13.3	3.4
20kg_5	20.6	1	–[a]	23.8	17.1	3.3
20kg_6	20.6	1	–[a]	22.8	16.5	2.9

[a] Not applicable due to complete failure of the specimen at first drop.

bottom extreme fiber of the plates is thus 100 times higher than for the uniaxial tensile tests. It corresponds to typical low velocity impacts such as vehicle impact or rock fall [20].

The results of the first drop for selected drop weight tests are shown in more detail in Fig. 9 with the labels of the curves corresponding to Table 2. The selected results represent the tests which provided the minimum and maximum response values.

The maximum measured acceleration after impact, recorded from the accelerometers affixed to the 20.6 kg weight was 50% smaller than for the 10.3 kg weight (120 g compared to 240 g). This led to maximum impact forces during the first drop were between F_{DW} = 22 and 26 kN occurring at approximately 1.6 ms after initial contact (Fig. 9a). The peak force was largely equal for all specimens. However, the post-peak response was influenced by the crack pattern and location of localized cracks.

Fig. 9b shows the mid-span deflection history of the plates during the first drop. Specimen 20kg_4 was one of the specimens which exhibited complete fracture during the first drop. For the plates impacted with the 10.3 kg weight, the maximum deflections were between −4.1 and −5.7 mm. Note that the maximum deflections for specimens impacted by the 20.6 kg weight were always larger than −6.5 mm.

Fig. 9c shows the sum of the vertical support reactions F_{su} versus time. The forces measured in the load cells under each support were similar, which confirmed symmetric specimen behavior. The reaction values were corrected for the initial prestress in the threaded bars. Positive values signify compression in the load cells during the test. The vertical support reactions became negative for several specimens, however, the uplift force was always lower than the initial prestress force, and no loss of contact with the supports occurred. The peak value of the sum of the support reactions occurred at 2.5 ms, approximately 0.9 ms after peak of the drop weight force F_{DW}. This was attributed to inertia and retardation effects in the specimen during the test.

The accelerations a_1 had maximum values of approximately 210 g for all specimens at 1.5 ms (Fig. 9d). The minimum value of a_1 was dependent on the applied drop weight: it was approximately −180 g for the specimens impacted with the 10.3 kg weight and −90 g with the 20.6 kg weight (Fig. 9d). Especially the specimens with low residual deformations, such as 10kg_2, showed pronounced oscillations in the value of acceleration after initial impact. For the specimens with higher residual deformations, such as 20kg_4, the accelerations stabilized quickly after initial impact around a value of zero. This was attributed to the higher inelastic energy dissipation in the specimens with higher residual deflections. A similar tendency was also observed in the damping of the deflection amplitude.

No cracks were observed on the upper surface of the specimens during visual inspections after each drop. All specimens showed very fine multiple cracks in the central portion of the lower surface, which are typically observed for strain hardening materials. The final fracture of the specimen occurred by fiber pullout in one localized crack which exhibited a very rough fracture surface. The failure mode for all specimens was in bending and identical to the quasi-static fracture mode.

Fig. 10a provides the evolution of deflected shape up to maximum deflection for the first drop of specimen 10kg_2. In comparison, the evolution of the strain at the bottom surface of the

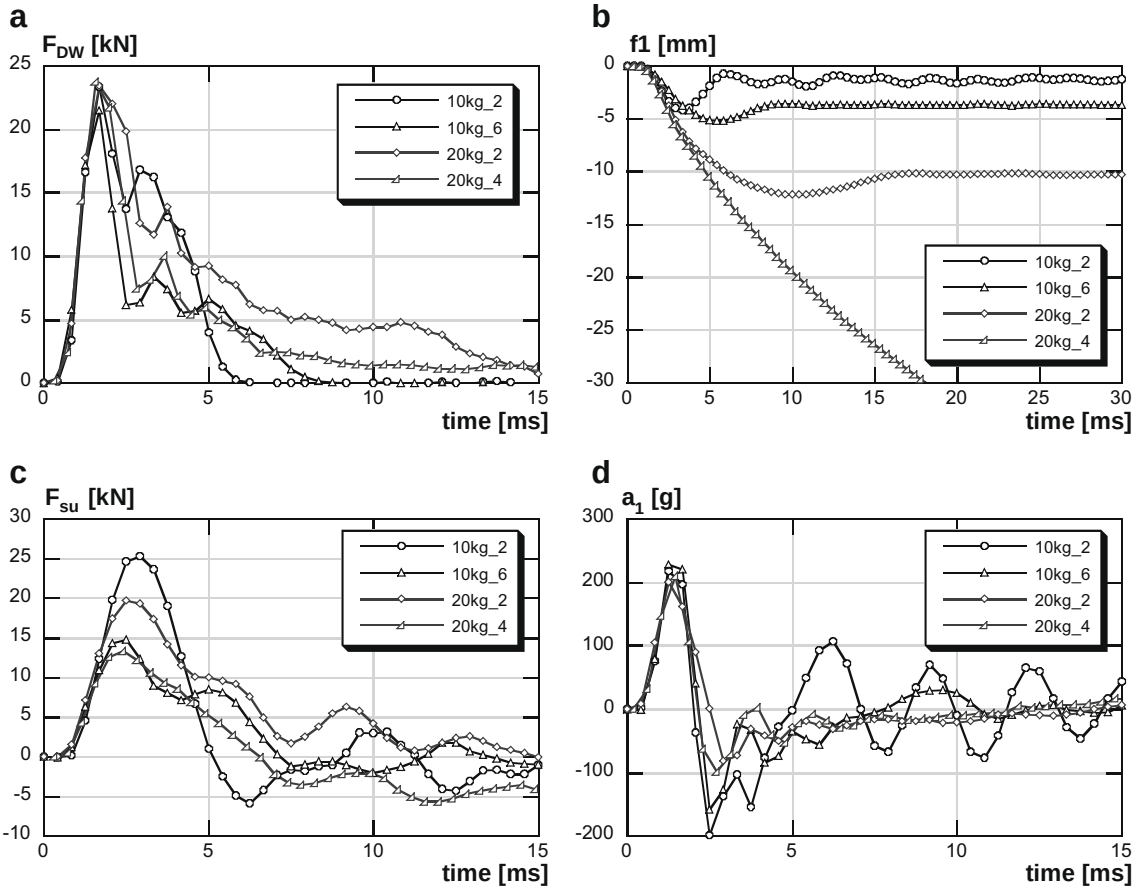

Fig. 9. Results of the drop weight tests: (a) drop weight force vs time, (b) mid-span deflection vs. time, (c) sum of the support reactions vs. time and (d) acceleration a_1 vs. time.

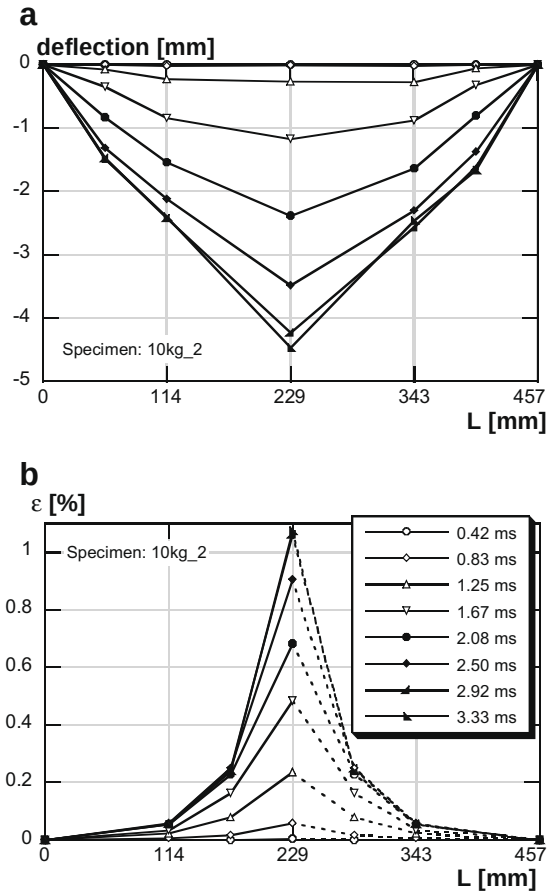

Fig. 10. First drop of specimen 10kg_2: evolution of (a) the deflected shapes and (b) the strain values at the bottom of the specimen with time (legend applies to both parts of the figure).

specimen is given for the same time span in Fig. 10b. The specimen was instrumented in the longitudinal direction with three 30 mm long strain gauges at mid-span and at 72 mm and 114 mm from the mid-span. Since only one side was instrumented, the shapes were mirrored to the other half of the specimen and are shown as dotted lines.

The deflected shapes were close to the elastic deflected shape until a mid-span displacement of −2.5 mm (Fig. 10a). For higher deflections, the shapes of deflection (Fig. 10a) and strain rates (Fig. 10b) were more pointed in the center, indicating inelastic deformations in the center region due to strain hardening and cracking in the specimen. No large cracks, however, were observed after the first drop. The maximum apparent strain at mid-span was $\varepsilon = 1\%$. The strain gauge at mid-span recorded a residual strain of 0.6% after the first drop for a residual mid-span deflection of −1.3 mm.

4.3.2. Analytical analysis and discussion

The deflection time history and the drop weight force time history were used to calibrate the nonlinear spring R_P in the mass–spring model consistent with Eqs. (2) and (3). The spring R_P corresponds to the force–deflection relationship for an equivalent static three-point bending test whereby the rate effect on the material properties is incorporated. Such a relationship, combined with the sectional bending model allowed determination of the equivalent uniaxial tensile material properties under dynamic loading.

4.3.2.1. Equivalent static bending behavior. The equivalent mass m_P was taken as 40% of the beam weight, representing the average m_P value corresponding to the linear–elastic response and the response assuming a hinge at mid-span using Eq. (1) [19,20].

A bi-linear spring function for the plywood R_D was determined from quasi-static test results on equivalent plywood samples as shown in Fig. 11. The average stress was multiplied by a factor of 1.3 to account for the change in material properties under dynamic loading according to [21]. The speed of the drop weight du_{DW}/dt at the time of impact was given as initial condition.

The UHPFRC plates were assumed to fail on the flexural tension side in accordance with the experimental observations. The maximum compressive strength was assumed to be $f_{Uc} = 150$ MPa to account for the dynamic increase in strength for the modeling.

The model was able to account for multiple impacts using the procedure graphically described in Fig. 12. This was achieved by defining a linear unloading and reloading path between impacts. Fig. 13 shows the drop weight force versus time and mid-span deflection $f1$ versus time curves of the upper and lower deflection values across the range of tests (specimens 10kg_6, 20kg_4 and 20kg_2). The second drops of specimens 10kg_2 and 20kg_2 were modeled by zeroing the deflections of the second drops according to Fig. 12.

The experimental drop weight force was assumed to correspond to the plywood spring force R_D and the experimental mid-span deflection was taken to be equal to the displacement u_P For all specimens, the model was able to reproduce duration of the drop weight force, peak force and shape of the force–time response as a function of time (Fig. 13). The model was also able to reproduce multiple impacts and thus, could predict the number of impacts

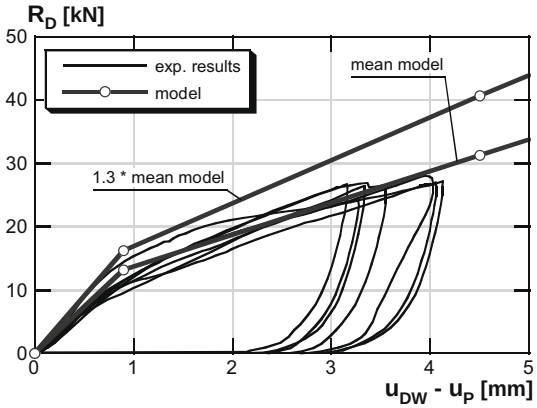

Fig. 11. Quasi-static force–displacement curve of the plywood.

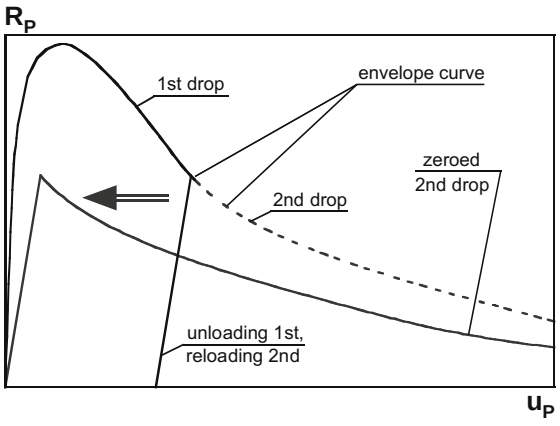

Fig. 12. Schematic procedure of the zeroing of spring R_P for multiple drops.

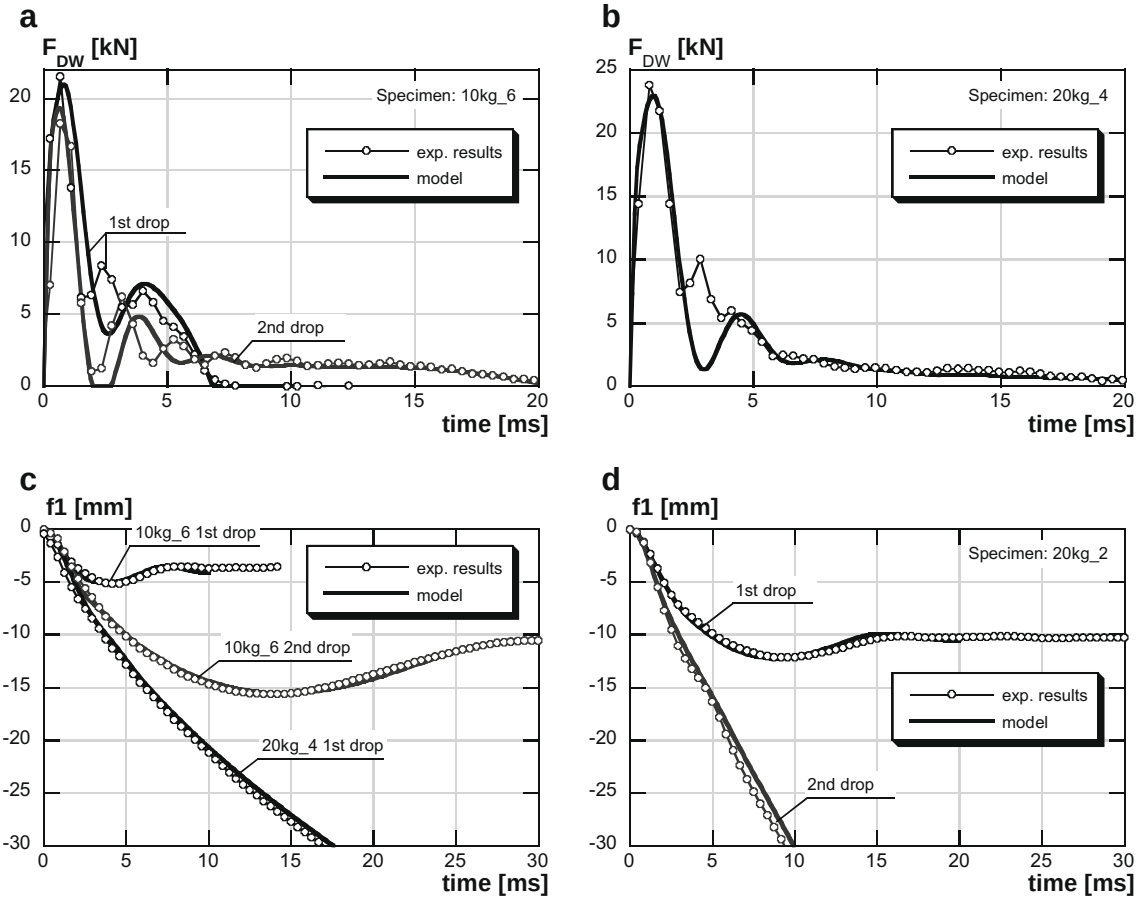

Fig. 13. Modeling of specimens 10kg_6, 20kg_4 and 20kg_2: (a) 10kg_6: F_{DW}–t, (b) 20kg_4: F_{DW}–t, (c) $f1$–t (10kg_6, 20kg_4) and (d) $f1$–t (20kg_2).

needed for final fracture when used in a design approach. Since the model does not account for changes in viscosity due to damping, only the first peak of deflection was modeled. Even though the data acquisition rate was relatively low, the modeling results suggested that there was no important loss in information.

The dynamic force–deflection curves obtained from the model were characterized by a higher maximum load than the mean curve obtained from measurements during the quasi-static tests (Fig. 14): the increase was between 25% for specimens 10kg_6, 20kg_4 and 70% for 20kg_2.

4.3.2.2. Equivalent static uniaxial tensile behavior. The uniaxial tensile behavior derived from the cross-sectional model is given in Fig. 15. Also, the test results of Fig. 5 are shown for comparison. The assumed hinge and reference lengths for modeling the two dynamic specimens was 100 mm and the reference length 120 mm identical to the values assumed for modeling the three-point bending quasi-static test results. The crack leading to failure of specimen 20kg_2 was 30 mm eccentric from the loading point. This eccentricity was added to the basic hinge length of 100 mm to result in a hinge length of 130 mm.

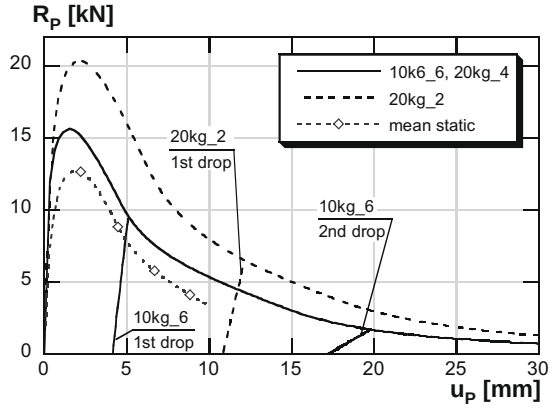

Fig. 14. R_P–u_P curves of specimens 10kg_6, 20kg_2 and 20kg_4.

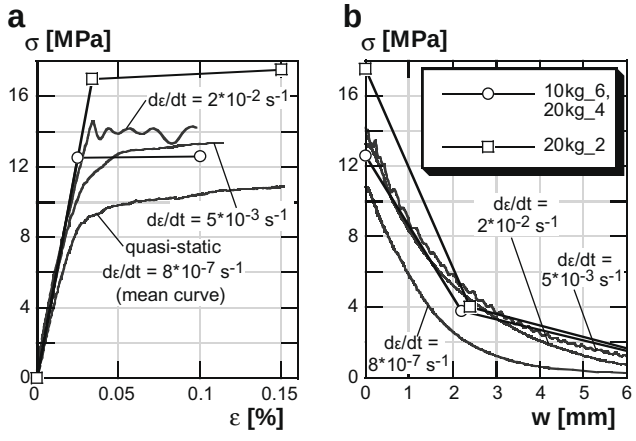

Fig. 15. Modeled uniaxial tensile behavior of specimens 10kg_6, 20kg_2, 20kg_4: (a) linear–elastic part and strain hardening and (b) softening.

Compared to the quasi-static behavior determined experimentally, the stress rise at the beginning of the modeled dynamic response was higher. This led to a higher modulus of elasticity of 60 GPa compared to a quasi-static modulus of elasticity of 40 GPa (Fig. 15a). Moreover, the modeled dynamic tensile strength was increased by 15% to f_{Ut} = 12.6 MPa for 10kg_6 and 20kg_4 and by 60% to f_{Ut} = 17.5 MPa for 20kg_2 when compared to the quasi-static experimental results. The modeled dynamic strain at the peak tensile strength was 0.1% and 0.15% for the modeled values and 0.15% for the quasi-static test results. This indicates that there was no significant loss in strain hardening for the specimens subjected to higher strain rates.

The softening behavior of the modeled drop weight specimens showed higher stress values for a given crack width w, when compared to the quasi-static test results (Fig. 15b). Modeling showed that the main difference of specimens 20kg_2 and 10kg_6 compared to 20kg_4 was observed in the first part of the softening region, while the second part was virtually identical for all dynamic tests. This suggests that the fiber pullout at larger crack openings was identical for all drop weight specimens.

5. Conclusions

The following conclusions can be drawn from this study on the behavior of UHPFRC under low and high strain rates and related analytical modeling:

1. Under quasi-static loading, the UHPFRC considered in this study exhibited strain hardening to an elongation of 0.15% and a tensile strength of 11.0 MPa. The tensile behavior determined from uniaxial tensile tests related well to tensile properties deduced from three- and four-point bending tests as shown with the proposed cross-sectional based analytical model. Note that there was some scatter due to variation in fiber orientation in the measured test results.
2. Drop weight and quasi-static bending tests had identical failure modes: multiple cracking was observed in the high moment region and final fracture occurred by fiber pullout in one localized bending crack at the center of the specimen.
3. An analytical two mass–spring model of the drop weight configuration was in good agreement with the impact test results. The modeling allowed determination of the equivalent static bending response. Also, the modeling technique permitted the simulation of multiple drops. The dynamic tensile behavior could then be determined by the cross-sectional based analytical model. Thus, the analytical modeling technique for the impact tests, adapted from [19,20], proved to be valid for the UHPFRC plate tests performed in this study.
4. The analysis showed that the UHPFRC strength increased with increasing strain rate, for strain rates $d\varepsilon/dt$ of up to 2 s^{-1}, the maximum considered in the present study. At this strain rate, the UHPFRC continued to exhibit strain hardening characteristics. Multiple cracking was also observed during testing. The bending resistance increased by more than 25% and the corresponding uniaxial tensile strength was increased by more than 15% relative to static behavior.
5. This study demonstrates that the advantageous properties of UHPFRC, such as its strain hardening behavior also subsist under high strain rates.

Acknowledgements

The authors would like to thank Prof. Eugen Brühwiler and his co-workers, who made it possible to conduct the uniaxial tensile tests at the Swiss Federal Institute of Technology at Lausanne. Discussions with Prof. P. Bischoff gave the authors valuable inspiration. Also, funding from the German Research Foundation (DFG) and the Natural Sciences and Engineering Research Council of Canada (NSERC), and material donations from Bekaert, Lafarge, MBT (BASF) and Elkem are gratefully acknowledged.

References

[1] Richard P, Cheyrezy M. Composition of reactive powder concretes. Cement Concr Res 1995;25(7):1501–11.
[2] Rossi P, Arca A, Parant E, Fakhri P. Bending and compressive behaviors of a new cement composite. Cement Concr Res 2005;35(1):27–33.
[3] Bache HH. Introduction to compact reinforced composite. Nordic Concr Res 1987;6:19–33.
[4] Charron, JP, Denarié, E, Brühwiler, E. Permeability of UHPFRC under high stresses. In: Proceedings RILEM symposium on advances in concrete through science and engineering, March 22–24, Chicago, USA, 2004 (CD-ROM).
[5] Lawler JS, Zampini D, Shah SP. Permeability of cracked hybrid fiber-reinforced mortar under load. ACI Mater J 2002;99(4):379–85.
[6] Brühwiler E, Denarié E, Putallaz J-Chr. Instandsetzung einer Betonbrücke mit ultrahochleistungsfähigem Faserfeinkornbeton (UHLFB). (Rehabilitation of a concrete bridge with UHPFRC). Beton- und Stahlbetonbau 2005;100(9):822–7.
[7] Alaee FJ, Karihaloo B. Retrofitting of reinforced concrete beams with CARDIFRC. ASCE J Compos Construct 2003;7(3):174–86.
[8] Krstulovic-Opara N, Dogan E, Uang CM, Haghayeghi AR. Flexural behavior of composite R.C.-slurry infiltrated mat concrete (SIMCON) members. ACI Struct J 1997;94(5):502–12.
[9] Kim JHJ, Lim YM, Won JP, Park H-G, Lee K-M. Shear capacity and failure behavior of DFRCC repaired RC beams at tensile region. Eng Struct 2007;29(1):121–31.
[10] Habel K, Denarié E, Brühwiler E. Experimental investigation of composite "UHPFRC-concrete" members. ACI Struct J 2007;104(1):93–101.
[11] Naaman AE, Gopalaratnam VS. Impact properties of steel fibre reinforced concrete in bending. Int J Cement Compos Lightweight Concr 1983;5(4):225–33.
[12] Maalej M, Quek ST, Zhang J. Behavior of hybrid fiber engineered cementitious composites subjected to dynamic tensile loading and projectile impact. ASCE J Mater Civ Eng 2005;17(2):143–52.
[13] Parant E, Rossi P. Damage mechanism of a multiscale fiber reinforced composite – I. Damage when submitted to pulsed loads. Bulletin des Laboratoires des Ponts et Chaussées, Paris, France, 2004, vol. 248. p. 73–81.
[14] Luo X, Sun W, Chan SYN. Steel fiber reinforced high-performance concrete: a study on the mechanical properties and resistance against impact. Mater Struct 2001;34(237):144–9.
[15] Zhang MH, Shim VPW, Lu G, Chew CW. Resistance of high-strength concrete to projectile impact. Int J Impact Eng 2005;31:825–41.
[16] Bindiganavile V, Banthia N, Aarup B. Impact response of ultra-high strength fiber reinforced cement composite. ACI Mater J 2002;99(6):543–8.
[17] Anderson WF, Watson AJ, Kaminskyi AE. The resistance of SIFCON to high velocity impact. In: Proceedings of structures under shock and impact II, SUSI/92, June 16–18, Portsmouth, UK, 1992. p. 89–98.
[18] Mayrhofer C. Response of reinforced SIFCON-slabs under blast-loading. In: Proceedings of structures under shock and impact III, SUSI/94, June 1–3, Madrid, Spain, 1994, p. 139–46.
[19] Biggs JM. Introduction to structural dynamics. New York: McGraw-Hill; 1964.
[20] CEB-FIP. Concrete structures under impact and impulsive loading. Synthesis Report, Bulletin d'information 187, Lausanne, Switzerland, 1988.
[21] Bischoff PH, Perry SH, Eibl J. Contact force calculations with a simple spring–mass model for hard impact: a case study using polystyrene aggregate concrete. Int J Impact Eng 1990;9(3):317–25.
[22] Schlüter FH. Dicke Stahlbetonplatten unter stoßartiger Belastung – Flugzeugabsturz (reinforced concrete slabs under impact-type loading). Heft 2, Schriftenreihe des Instituts für Massivbau und Baustofftechnologie, University of Karlsruhe, Germany, 1987.
[23] Habel K, Charron JP, Braike S, Hooton RD, Gauvreau P, Massicotte B. UHPFRC mix design in Central Canada. Can J Civ Eng 2008;35(2):217–24.
[24] Habel K, Viviani M, Denarié E, Brühwiler E. Development of the mechanical properties of an ultra-high performance fiber reinforced concrete (UHPFRC). Cement Concr Res 2006;36(7):1362–70.
[25] Denarié E, Brühwiler E. Tailored composite UHPFRC-concrete structures. In: Proceedings of measuring, monitoring and modeling concrete properties (MMMCP), ECF-16, S.P. Shah symposium, Alexandroupolis, Greece, July, 2006.
[26] Habel K, Gauvreau P. Impact behavior of concrete bridge deck slabs with composite ultra-high performance fiber reinforced concrete (UHPFRC) overlay. In: Proceedings 7th international conference on short & medium span bridges, Montreal, Canada, August 23–25, 2006 (CD-ROM).
[27] Habel K, Denarié E, Brühwiler E. Structural response of slabs combining ultra-high performance fiber reinforced concretes (UHPFRC) and reinforced concrete. ASCE J Struct Eng 2006;132(11):1793–800.